AGU ADVANCING EARTH AND SPACE SCIENCES

Earth and Space Science

RESEARCH ARTICLE
10.1029/2025EA004433

Sinking Airports: A Glance at the State of US Transport Infrastructure

Oluwaseyi Dasho[1] and **Manoochehr Shirzaei**[1,2]

[1]Department of Geosciences, Virginia Tech, Blacksburg, VA, USA, [2]United Nations University, Institute for Water, Environment and Health, Richmond Hill, ON, Canada

Key Points:

- Differential subsidence is detected along US airport runways
- Uneven ground deformation along runways poses serious risks to infrastructure stability and aircraft operations
- Interferometric Synthetic Aperture Radar technique offers a scalable solution for runways' health monitoring

Supporting Information:

Supporting Information may be found in the online version of this article.

Correspondence to:

O. Dasho,
seyidasho@vt.edu

Citation:

Dasho, O., & Shirzaei, M. (2025). Sinking airports: A glance at the state of US transport infrastructure. *Earth and Space Science*, *12*, e2025EA004433. https://doi.org/10.1029/2025EA004433

Received 18 APR 2025
Accepted 7 JUL 2025

Author Contributions:

Conceptualization: Oluwaseyi Dasho, Manoochehr Shirzaei
Formal analysis: Oluwaseyi Dasho, Manoochehr Shirzaei
Funding acquisition: Manoochehr Shirzaei
Investigation: Oluwaseyi Dasho
Visualization: Oluwaseyi Dasho
Writing – original draft: Oluwaseyi Dasho
Writing – review & editing: Oluwaseyi Dasho, Manoochehr Shirzaei

Abstract Land subsidence poses a growing challenge to the operational safety and structural integrity of global air transport infrastructure. This study assesses the impact of differential land subsidence on airport runways using cutting-edge Interferometric Synthetic Aperture Radar (InSAR) data across 15 major U.S. airports, providing an estimate of potential foundational damage caused by settlement due to natural and anthropogenic factors. Our findings show San Francisco International Airport experiences the fastest subsidence rate of 9.2 ± 0.2 mm/year, while Los Angeles International Airport has the slowest subsidence rate of 2.0 ± 0.2 mm/year. While 96.1% of runway areas fall under low damage risk, 3.9% are at medium to very-high (VH) risk, with 3.5 million m^2 exposed to subsidence rates exceeding 5 mm/year and 13,950 m^2 classified as being at high to VH damage risk. Although no accidents have been directly linked to subsidence, increasing maintenance costs underscore the need for proactive monitoring. InSAR provides a near real-time, cost-effective solution for detecting infrastructure vulnerabilities, offering a non-intrusive approach to enhancing airport resilience and operational safety.

Plain Language Summary Airports are increasingly challenged by uneven ground sinking along runways, also known as differential land subsidence, which can damage runways and affect flight operation. This study uses advanced satellite technology called InSAR (Interferometric Synthetic Aperture Radar) to measure how much the ground is sinking at 15 major U.S. airports. We found that San Francisco International Airport is sinking the fastest-about 9.2 mm per year, while Los Angeles International Airport has the slowest sinking rate at 2 mm per year. Although most runway areas (over 96%) are currently at low risk, about 3.9% of runway surfaces are at moderate to very-high risk of damage from sinking ground. This includes 3.5 million square meters of runway experiencing significant sinking, and nearly 14,000 square meters at high risk of structural damage. So far, no crashes or major incidents have been directly caused by subsidence, but airports are facing higher maintenance costs as they try to fix damage. Our study shows that using InSAR can help airport managers monitor runway conditions in near real time and spot problems early, helping to improve safety and reduce repair costs.

1. Introduction

Differential subsidence, the uneven settling of the ground due to geotechnical, hydrological, and climatic factors, poses a critical threat to global infrastructure systems (Davydzenka et al., 2024; Lenardón Sánchez et al., 2024; Zaenal Putra et al., 2024). This phenomenon is predominantly driven by soil compaction (Mohseni & Bol, 2021), groundwater extraction (Smith & Majumdar, 2020), seismic activity (Albano et al., 2024), seasonal frost heave (Robson et al., 2021; Rouyet et al., 2019), and permafrost degradation (Valman et al., 2024), some of which are projected to intensify in some regions due to climate change, leading to structural deformation, increased maintenance costs, and potential service disruptions. For instance, in megacities such as Shanghai, Jakarta, and Mexico City, historical subsidence rates have exceeded 10 cm per year, severely impacting buildings, bridges, roads, railways, runways and underground utilities (Abidin et al., 2015; Cigna & Tapete, 2021; Fernández-Torres et al., 2020; Li et al., 2021). Airports represent high-risk assets among exposed infrastructures due to their stringent operational and safety requirements. In particular, airport runways demand strict elevation uniformity and minimal deformation tolerance, as even minor surface irregularities can compromise aircraft performance, braking efficiency, and overall flight safety. Subsidence along runways can lead to widespread cracking (Mehta et al., 2017), increased slipperiness due to water accumulation (Huseby & Rabbe, 2018), drainage problems, surface roughness (Gerardi, 2007), and slope changes, all of which can negatively impact runway performance and compromise air travel safety.

Table 1
Various Infrastructure Monitoring Methods, Including Their Pros and Con

Method	Advantages	Disadvantages
Extensometers	Accurate measurement of vertical displacement at specific locations.	Limited to point-based measurements, requires multiple installations
GNSS	High accuracy for both horizontal and vertical displacement.	Expensive setup, requires network of stations for extensive coverage
Leveling Surveys	Precise elevation changes, widely used in civil engineering	Time-consuming, labor-intensive, limited spatial coverage.
InSAR	High spatial coverage, remote sensing with minimal disruption.	Subject to atmospheric and topographic errors, needs advanced processing.
Ground Penetrating Radar	Non-invasive detection of subsurface features, useful for structural analysis.	Limited depth penetration, less effective in water-rich or conductive soils.
Optical Surveys	Low cost, easy deployment, suitable for quick surface deformation assessments.	Less accurate, requires line-of-sight and good weather conditions.
Fiber Optic Sensors	Real-time continuous monitoring, high sensitivity, monitors long distances.	High installation costs, complex setup, sensitive to environmental noise.

Airport infrastructure maintenance is more critical than ever in the climate change era, as airports increasingly contend with extreme weather events, rising sea levels, and evolving environmental conditions. Ensuring the resilience of critical infrastructure is essential for maintaining operational safety, efficiency, and long-term sustainability. Traditional ground deformation surveys, such as GNSS and leveling surveys (Table 1), provide valuable insights into infrastructure health. While these methods offer high precision, their effectiveness is limited by restricted spatial coverage, high costs, and operational constraints, often requiring ground-based instrumentation that can disrupt airport operations (Fergason et al., 2015; Sato et al., 2003; Zheng et al., 2024). The advent of satellite-based Interferometric Synthetic Aperture Radar (InSAR) provides an unprecedented opportunity to overcome these challenges through high-resolution, continuous, and cost-effective deformation monitoring without the need for ground instrumentation (An et al., 2023; Ciampoli et al., 2020; Dai et al., 2020; Gagliardi et al., 2021; Galloway et al., 2000; Jiang et al., 2008; Miller & Shirzaei, 2019; Ohenhen et al., 2023; Zhuo et al., 2020). Integrating InSAR into routine maintenance and risk mitigation strategies offers a scalable and cost-effective solution.

Some other studies have used InSAR to investigate localized runway settlement (An et al., 2023; Cavalié et al., 2015; Dai et al., 2020; Gao et al., 2019) but the broader integration of InSAR for systematic, multi-site airport monitoring has yet to be fully explored. This study applies InSAR-derived vertical land motion (VLM) estimates to evaluate subsidence-induced damage risks across 15 major U.S. airports (Figure 1). By leveraging the multi-year Sentinel-1 SAR observations and advanced deformation risk assessments, we present a robust early warning system capable of detecting and quantifying structural vulnerabilities before they compromise aviation safety and infrastructure performance. To enhance accuracy and reliability, we incorporate GNSS validation and uncertainty quantification, ensuring consistency between independent data sets and satellite-derived estimates. This study evaluates subsidence-induced damage risks at 15 major U.S. airports (Figure 1; Table S1 in Supporting Information S1), which collectively served ~643 million passengers in 2024. as shown in Figure 1. Using these measurements, we derived the distortion angle parameter, a measure of allowable bending before failure initiation, used to assess potential damage risk. We estimate that about 3.5 million m^2 and 13,950 m^2 are exposed to subsidence and high to very-high (VH) damage risks, respectively.

2. Materials and Methods

2.1. Monitoring Subsidence Along Runways Using SAR Interferometry

This study analyzed 1,646 Sentinel-1A/B SAR images in the ascending direction to observe ground deformation along 15 airport runways (Table S2 in Supporting Information S1). High-resolution time series of Line-Of-Sight

10.1029/2025EA004433

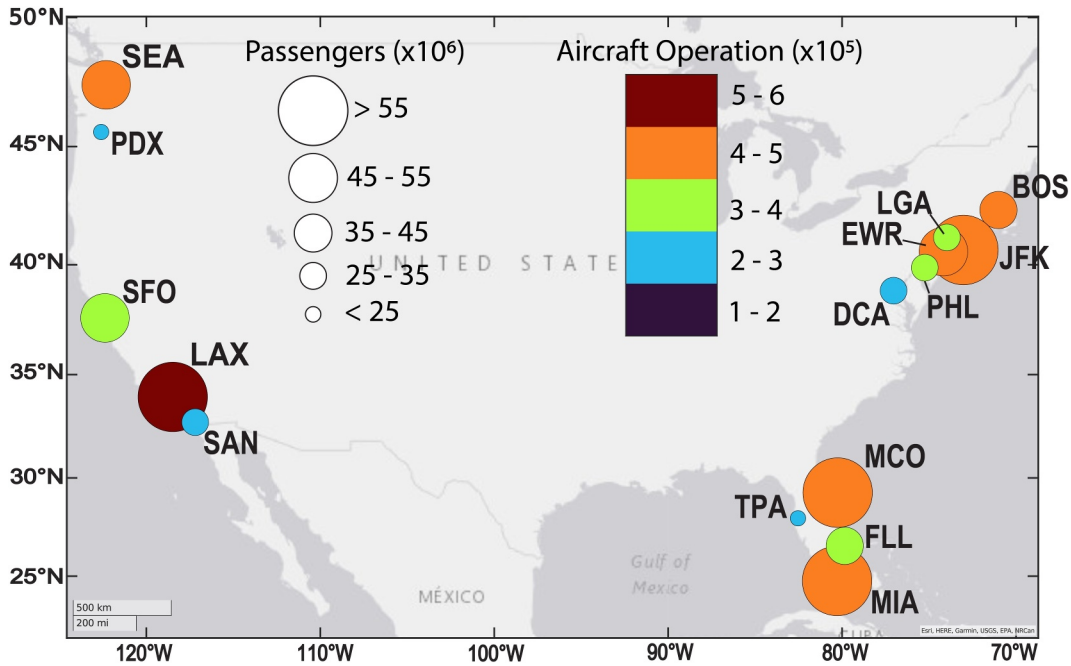

Figure 1. Geographic distribution of major U.S. airports with air traffic volume and passenger load statistics. Circle size represents total annual passengers (millions) while color scale represents aircraft operations (hundreds of thousands of flights per year) in the year 2024. Details in Table S1 in Supporting Information S1.

(LOS) displacement over each airport were derived (Figure S1 in Supporting Information S1) from the data set using the so-called Wavelet-based InSAR time series algorithm (Lee & Shirzaei, 2023; Shirzaei, 2013; Shirzaei & Bürgmann, 2012; Shirzaei et al., 2017).

We applied multi-looking factors of 6 (range) by 1 (azimuth) to obtain a pixel size of ∼15 × ∼15 m. Sets of interferometric triplets, comprising interferograms with a variety of temporal baselines, are produced using the Delaunay Triangulation method and dyadic down sampling to minimize the influence of phase closure error (Lee & Shirzaei, 2023). We generated a total number of 9,659 interferograms. We used the 30-m resolution Shuttle Radar Topography Mission Digital Elevation Model (Farr et al., 2007) and precise satellite orbital information to calculate and eliminate the impact of topographic phase and flat earth correction (Franceschetti & Lanari, 1999). We applied a 2D minimum cost-flow algorithm (Mario Costantini, 1998) to a sparse set of elites (i.e., less noisy pixels) (Costantini & Rosen, 1999) to estimate absolute phase changes. To produce the LOS time series of displacement for each pixel, the unwrapped phase values of interferograms were combined by applying a reweighted least-squares approach (Shirzaei, 2013). To compute and reduce the atmospheric delay in the SAR interferometry, we applied 2D smoothing splines (Lee & Shirzaei, 2023) and wavelet-based filters (Shirzaei & Bürgmann, 2012). LOS mean rates, the slope of best-fitting lines of each pixel's time series, are projected to the vertical direction using the local incidence angle, assuming horizontal displacement can be approximated using a plane and then removed. The standard deviation of the VLM is presented in Figure S2 in Supporting Information S1.

To convert the InSAR-based VLM measurements from a local reference frame to the standard IGS14 global reference frame, we used the global VLM model created by (Hammond et al., 2021). Their model captures large-scale VLM signals from effects like glacial isostatic adjustment (GIA), tectonics, and water storage changes across the whole globe. We implemented an affine transformation to align the localized InSAR VLM data set with the global IGS14 coordinate system (Blackwell et al., 2020; Ohenhen et al., 2023). The affine transformation accounts for rotations, offsets and scaling differences between the InSAR local and the global IGS14 reference frame. This process integrated InSAR measurement into the broader global spatial reference frame for consistent cross-comparison and analysis.

2.2. Estimation of Subsidence Acceleration

Including an acceleration term accounts for temporal variations in VLM, capturing temporal variability of subsidence or uplift rates. To this end, we fitted a parabolic function to the displacement time series. The displacement time series, $\varphi(t)$, representing vertical ground movement at a given location, is expressed by a second-order polynomial function:

$$\varphi(t) = v_0(t - t_0) + \frac{1}{2}a(t - t_0)^2 + C + \epsilon \tag{1}$$

Where v_0 (mm/year) is the initial velocity (different from mean velocity), a (mm/year^2) is the vertical acceleration, t is the time in years, t_0 (years) is the reference time, set as the earliest observation in the data set, C is a constant and ϵ is the observation residual.

Equation 1 was rewritten in matrix form:

$$\boldsymbol{\Phi} = \boldsymbol{B}\Delta + \boldsymbol{\epsilon} \tag{2}$$

where, $\boldsymbol{\Phi} = [\varphi(t_1), \varphi(t_2), \ldots, \varphi(t_n)]^T$ is the vector of observed n vertical displacements,

$$\boldsymbol{B} = \begin{bmatrix} t_1 - t_0 & \frac{1}{2}(t_1 - t_0)^2 & 1 \\ t_2 - t_0 & \frac{1}{2}(t_2 - t_0)^2 & 1 \\ \vdots & \vdots & \vdots \\ t_n - t_0 & \frac{1}{2}(t_3 - t_0)^2 & 1 \end{bmatrix} \tag{3}$$

$$\Delta = \begin{bmatrix} v_0 \\ a \\ C \end{bmatrix} \tag{4}$$

Given the vertical displacement time series, the unknown vector Δ is estimated via least squares optimization at each observation point within the study area.

2.3. Distortion Angle

In geotechnical engineering, the angular change in relative elevation of two adjacent points, so-called angular distortion, is widely used to indicate infrastructure damage due to differential settlement (Burland & Wroth, 1975; Cigna & Tapete, 2021; Fernaoóndez-Torres et al., 2020; Vassileva et al., 2021). Given two observation points apart by horizontal distance l and settlements of δ_1 and δ_2, the angular distortion, β is given by Equation 1:

$$\beta = \frac{\delta_2 - \delta_1}{l} \tag{5}$$

Given the *jth* InSAR pixel at a location (x_j, y_j) and m adjacent pixels (x_i, y_i) and associated subsidence rates of δ_i, where $i = 1, \ldots, m$, we employ a planar strain field, approximating the local subsidence field by equation (6)

$$\delta = ax + by + c \tag{6}$$

Using matrix notations, assuming observation vector $\boldsymbol{L}$ and unknown vector $\boldsymbol{X}$, equation (6) can be rewritten as

$$\boldsymbol{L} = \boldsymbol{AX} + \boldsymbol{v} \tag{7}$$

where

$$\boldsymbol{L} = [\delta_1, \delta_2, \ldots, \delta_m]^T$$
$$\boldsymbol{X} = [a, b, c]^T \tag{8}$$
$$\boldsymbol{A} = \begin{bmatrix} x_j & y_j & 1 \\ x_1 & y_1 & 1 \\ \vdots & \vdots & \vdots \\ x_m & y_m & 1 \end{bmatrix}$$

And $\boldsymbol{v}$ is the vector of observation residuals. A solution to Equation 3 can be obtained through least squares optimization (Mikhail & Ackermann, 1982). The angular distortions at location (x_j, y_j) in x and y directions, β_x and β_y and total angular distortion β are defined as

$$\beta_x = \frac{d\delta}{dx} = a$$
$$\beta_y = \frac{d\delta}{dy} = b \tag{9}$$
$$\beta = \sqrt{\beta_x^2 + \beta_y^2}$$

Figure S3 in Supporting Information S1 shows the distribution of calculated β for each airport. Depending on the type of materials, a range of β is suggested as an indicator for negligible to severe infrastructure damage due to differential subsidence. For instance, (Wood, 1958) reported cracks and damage to brick walls and encased steel frames for a β of 1/1,000 to 1/100. Also, β greater than 6.6/1,000 is associated with structural damage in beams and columns (Skempton & MacDonald, 1956), and β larger than 3.3/1,000 can cause cracking in structures with steel or reinforced concrete frames (Cigna & Tapete, 2021; Day, 1990). To estimate the runway areas at risk of damage due to differential subsidence, we scale the estimated β to the length of the observation period to obtain β_{tot} and, following (Cigna & Tapete, 2021; Ohenhen & Shirzaei, 2022), define four risk classes of low ($0 \leq \beta_{\text{tot}} < 1/3{,}000$), medium ($1/3{,}000 \leq \beta_{\text{tot}} < 1/1{,}500$), high ($1/1{,}500 \leq \beta_{\text{tot}} \leq 1/500$), and VH ($\beta_{\text{tot}} > 1/500$), indicative of the increasing likelihood of damage.

3. Results

3.1. Land Subsidence Along Airport Runways

Figure 2 shows the VLM rates with respect to the IGS14 global reference frame along runways, with negative values indicating subsidence. Figure 2a presents the average subsidence rate at each airport, weighted by the spatial extent of subsiding areas within the airport boundary. Among all the airports analyzed, SFO exhibits the highest area-weighted subsidence rate. Figure 2b shows the total area and percentage area of the runway experiencing subsidence. About 75% of the total runaway area in Miami International Airport (MIA) and PHL is undergoing varied degrees of subsidence. The box plots in Figure 2c represent the distribution of VLM at each airport with the central lines indicating median VLM while the boxes show the interquartile range.

To validate the VLM estimates from InSAR, we compared the estimates with the vertical displacement rate from GNSS stations that fall within the spatial extent of the InSAR data set. The GNSS data were provided by the Nevada Geodetic Laboratory (Blewitt et al., 2016). To obtain InSAR-based VLM at the location of each GNSS station, we averaged pixels within 50 m of each station. Figure 3 shows the bivariate plot comparing the InSAR-based and GNSS vertical measurements. The two data sets show good agreement in their measurements with an R^2 of 0.81.

Figure 4 presents the spatial distribution of VLM across runways in all 15 airports studied. In the following, we discuss the results in three distinct geographic regions.

10.1029/2025EA004433

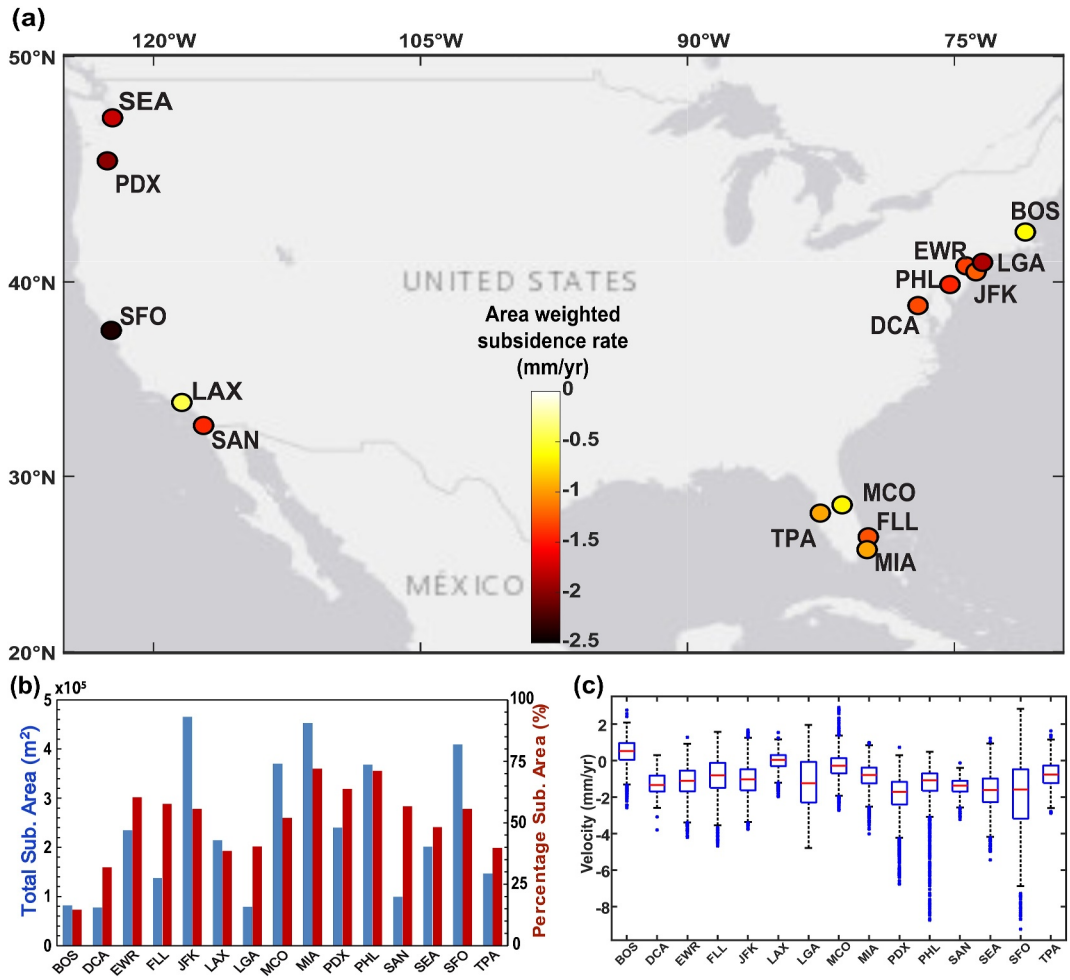

Figure 2. Vertical land motion (VLM) along runways of studied airports. (a) The map shows the area-weighted subsidence rates (in mm/year) across the studied coastal airports in the United States. Each airport is marked with a circle color-coded to their area-weighted subsidence rates (b) the bar chart displays the total area affected by subsidence (blue bars) and the percentage of subsiding areas relative to the total airport area (red bars). (c) The boxplot illustrates the range of VLM velocities distribution at the studied airports. Negative values indicate subsidence, while positive values indicate uplift. The red line indicates the median VLM rate, while the blue box represents the interquartile range. Whiskers denote the 5th–95th percentile range.

3.1.1. Northeast Corridor Airports

The Northeast Corridor airports share distinctive geological characteristics, with most facilities constructed on reclaimed wetlands, coastal fill, and glacial deposits. The entire region is affected by a slow subsidence rate due to GIA (Ohenhen et al., 2024). While the localized VLM pattern at each airport is spatially varying, often alternating between uplift and subsidence. The region contains both the airport with the highest total subsiding area (JFK at 465,300 m^2) and the lowest (DCA at 77,625 m^2) (Figure 2b) among airports considered in this study. Median VLM rates in this region range from −1.0 mm/yr to 0.5 mm/yr, with BOS showing the highest median value (0.5 mm/yr) among all airports studied (Figure 2c). Figure 4a presents a complex pattern of alternating uplift and subsidence across BOS's six-runway system, reflecting the heterogeneous nature, both composition and thickness, of its reclaimed land foundation. EWR exhibits subsidence along runway 11–29, particularly at the northwestern end where rates reach −4.2 ± 0.2 mm/yr (Figure 4c), likely reflecting differential settlement of reclaimed wetland areas with varying thicknesses of compressible organic soils; the area-weighted subsidence across EWR runways is −1.1 mm/yr (Figure 2a), with approximately 60.4% of total runway area experiencing subsidence, while runways 4L-22R and 4R-22L show more variable vertical motion patterns alternating between

10.1029/2025EA004433

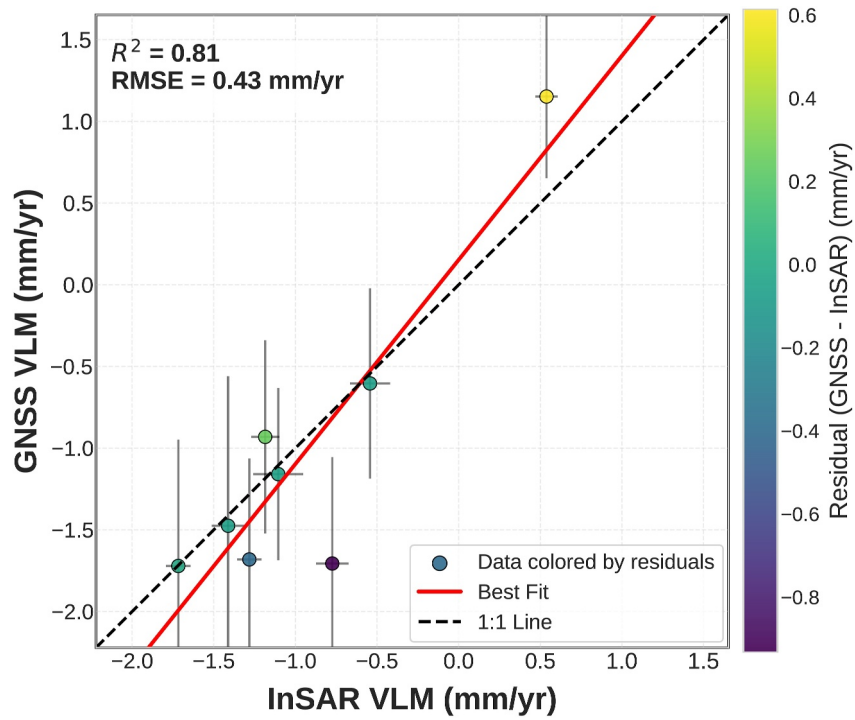

Figure 3. Bivariate plot comparing the GNSS vertical displacement and InSAR-based vertical land motion rates, yielding a R^2 of 0.81. The Interferometric Synthetic Aperture Radar uncertainties represent aggregated pixel-based averages.

uplift and subsidence. Figure 4e presents distinct subsidence patterns along all runways at JFK, likely reflecting ongoing consolidation of organic marsh deposits beneath the artificial fill used for airport construction.

LaGuardia Airport (LGA) and PHL (Figures 4g and 4k) both reveal variable VLM patterns alternating between uplift and subsidence, with LGA's 13–31 runway showing significant subsidence. While at DCA (Figure 4b), the runway 1–19 exhibits contrasting vertical movement toward both ends of the runway, which may lead to slope changes over time. The consistent pattern of varying VLM across Northeast Corridor airports reflects the complex geological foundation of this region, where glacial deposits, compressible marine clays, and artificial fill materials interact to create heterogeneous subsidence responses. The InSAR measurements reveal that airports built on thicker deposits of compressible materials (JFK, EWR) generally exhibit higher subsidence rates and more extensive affected areas than those constructed on more stable geological foundations. These observations highlight the importance of considering local geological variations when assessing infrastructure vulnerability, as even within the same regional context, significant differences in subsidence patterns emerge based on site-specific conditions and construction history.

3.1.2. Southeast Airports

Southeastern airports, located in areas underlain by limestone and influenced by karst processes, exhibit subsidence vulnerabilities that differ fundamentally from those caused by sediment compaction in other regions. These geologic conditions can lead to localized ground instability, including sinkhole formation, posing unique challenges to infrastructure resilience and long-term operational safety. Across these airports, moderate subsidence rates and complex spatial patterns reflect the heterogeneous nature of the underlying karst geology. Figure 4i presents the VLM along runways at MIA showing subsidence along its east-west trending runways 8L-26R and 8R-26L, with an area-weighted subsidence rate of −1.0 mm/yr (Figure 2a) and peak rates reaching −4.0 ± 0.1 mm/yr (Figure 2c); with a notably high 72% of its total runway area affected (Figure 2b), underscoring the challenges of building on South Florida's karst-prone limestone geology and organic soil deposits. Similarly, FLL displays moderate subsidence (Figure 4d), with more pronounced deformation at 28L and a pattern of opposing vertical deformation at both ends of the 10R-28L runway, indicating possible gradual alteration of the runway slope. MCO exhibits spatially varying vertical motion along its runway (Figure 4h), while at TPA,

10.1029/2025EA004433

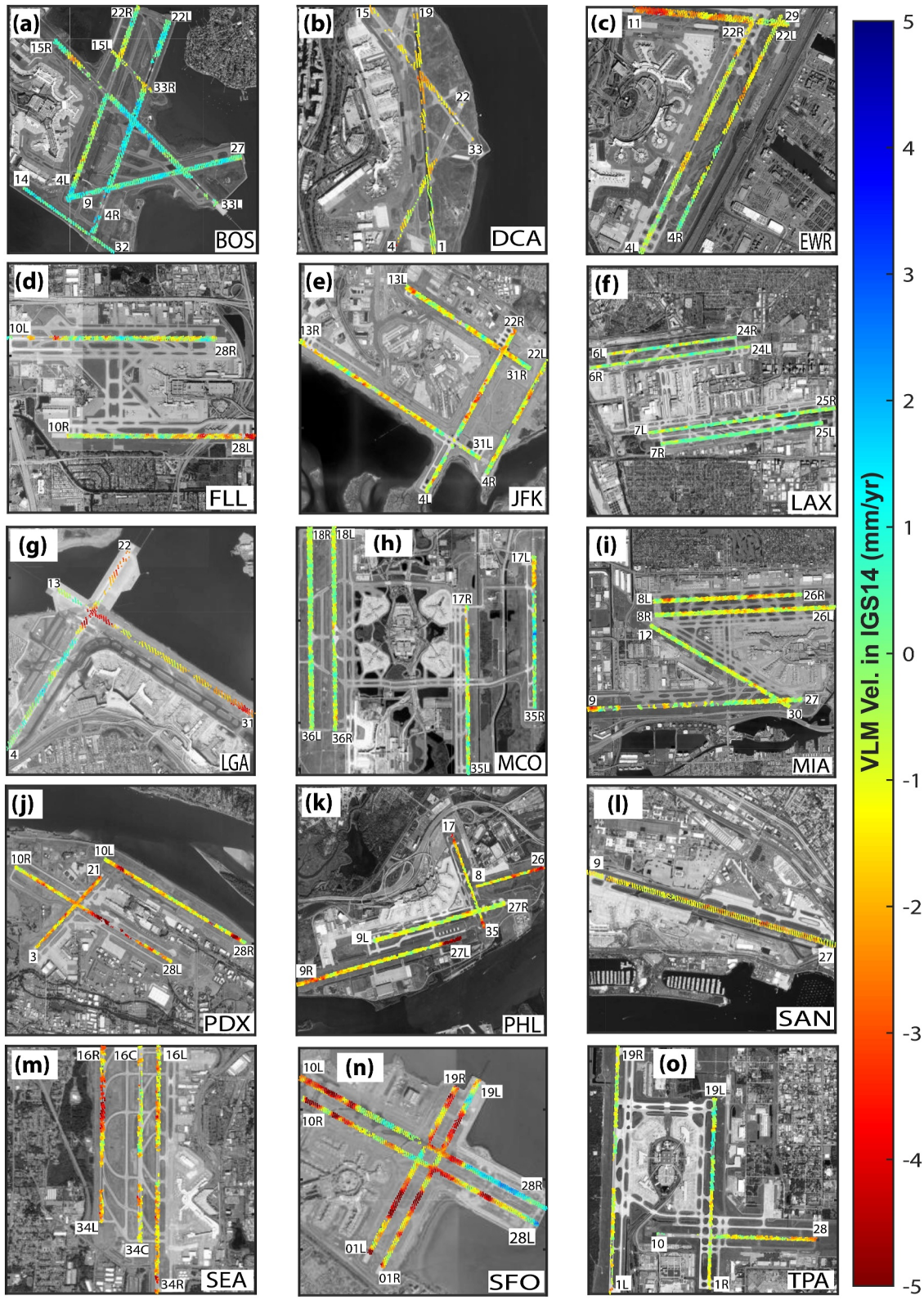

Figure 4. High-resolution satellite imagery overlaid with detailed vertical land motion (VLM) velocity data along runways for 15 major U.S. airports. Each subfigure (a–o) represents an airport, with colored gradients corresponding to subsidence or uplift (scale bar at the bottom). The colorbar represents VLM in mm/year, ranging from −5 mm/year (red, indicating subsidence) to +5 mm/year (blue, indicating uplift). Each airport panel includes runway labels and a grayscale ESRI satellite image for geographic reference.

subsidence is particularly pronounced along runway 10–28 (Figure 4o). The other runways at TPA demonstrate varying subsidence rates, likely influenced by heterogeneities within the underlying limestone bedrock. These observations underscore the significant role of karst processes, groundwater dynamics, and subsurface geological variability in infrastructure stability at airports across the Southeast region.

3.1.3. West Coast Airports

West Coast airports span diverse geological settings from reclaimed bay lands to alluvial valleys, exhibiting the greatest regional variation in subsidence rates, from the highest area-weighted subsidence rate (SFO at −2.4 mm/yr) to the lowest (LAX at −0.5 mm/yr) (Figure 2a). SFO experiences substantial subsidence across all four runways, with a maximum rate of -9.2 ± 0.2 mm/yr—the highest among all airports studied, with extensive areas of orange to red coloration (Figure 4n) indicating significant subsidence particularly along runways 1L-19R and 1R-19L; approximately 55.7% of total runway area is subsiding, with the two northeast-southwest trending runways showing the most severe subsidence while the northwest-southeast trending 10L-28R runway indicates some uplift toward its southeastern end. These subsidence patterns reflect the high compressibility of marine clay deposit underlaying SFO. Figure 4j shows significant subsidence across all three runways at PDX with a maximum rate of -6.8 ± 0.2 mm/yr and an area-weighted subsidence rate of −2.0 mm/yr (Figure 2a), with each runway exhibiting distinctive subsidence patterns: along 10L-28R, high subsidence is localized at both ends; along 10R-28L, it is concentrated at the midpoint; and along 3–21, it extends throughout the runway length, with approximately 63.8% of the total runway area subsiding, reflecting PDX's location on compressible floodplain deposits.

SEA exhibits variable subsidence patterns across its three parallel runways with a maximum rate of -5.4 ± 0.1 mm/yr and an area-weighted subsidence rate of −1.8 mm/yr (Figure 2a), with approximately 48.2% of the total runway area subsiding (Figure 2b), the highest subsidence zone is observed along runway 16R-34L. SAN shows a gradient in subsidence rate along its single runway 9–27 (Figure 4l), with rates increasing toward the eastern end and a visible transition from yellow to orange and red coloration. LAX has both the lowest area-weighted subsidence rate (−0.5 mm/yr) in this region and the lowest peak subsidence rate (-2.0 ± 0.2 mm/yr) among all airports studied, with predominantly green coloration (Figure 4f) along LAX's runways indicating very mild subsidence relative to other airports and a relatively uniform vertical motion pattern across all four parallel runways suggesting consistent geological conditions throughout the airport area, likely due to its construction on more stable alluvial sediments over marine terrace deposits rather than compressible bay mud or floodplain materials seen at other West Coast airports.

3.2. Profile Analysis

Figure 5a–5d presents temporal variability of the vertical displacement along selected runways at four major U.S. airports—BOS 9–27 runway (Figure 5a), JFK 4R-22L runway (Figure 5b), MIA 12–30 runway (Figure 5c), and SFO 10R-28L runway (Figure 5d)—demonstrating progressive changes in surface elevation. The magnitude and trends of displacement vary significantly among the airports, reflecting differences in geological, environmental, and infrastructural factors. The SFO 10R-28L runway shows the largest displacement, ranging from −3 cm to +1 cm over the period 2017 to 2021. Notably, there is a progressive elevation loss at specific segments, including 0.1 km, 0.5 km, 2.1 km, and 2.8 km from the starting point, potentially indicating localized geophysical processes. This pattern contrasts with the BOS 9–27 runway, where displacement is generally confined to the −1 to +1 cm range for period 2015 to 2021, suggesting more stable conditions.

At JFK 4R-22L runway, displacement remains relatively stable over time, as the profiles from recent years closely align with those of earlier years, highlighting minimal temporal variability. The MIA 12–30 runway exhibits a mix of subsidence and rebound patterns, with some recovery in elevation observed over time. Both BOS and MIA display cyclical trends of subsidence and uplift along specific segments, potentially indicative of seasonal effects. Cross-sectional profiles of all the runways show the variability of ground deformation along the runways with time (Figures S4–S18 in Supporting Information S1).

3.3. Subsidence Acceleration Along Runways

Figure 6 presents the spatial distribution of acceleration (positive) and deceleration (negative) at subsiding areas along the 15 major U.S. airport runways, highlighting areas where the subsidence rate potentially increases or

10.1029/2025EA004433

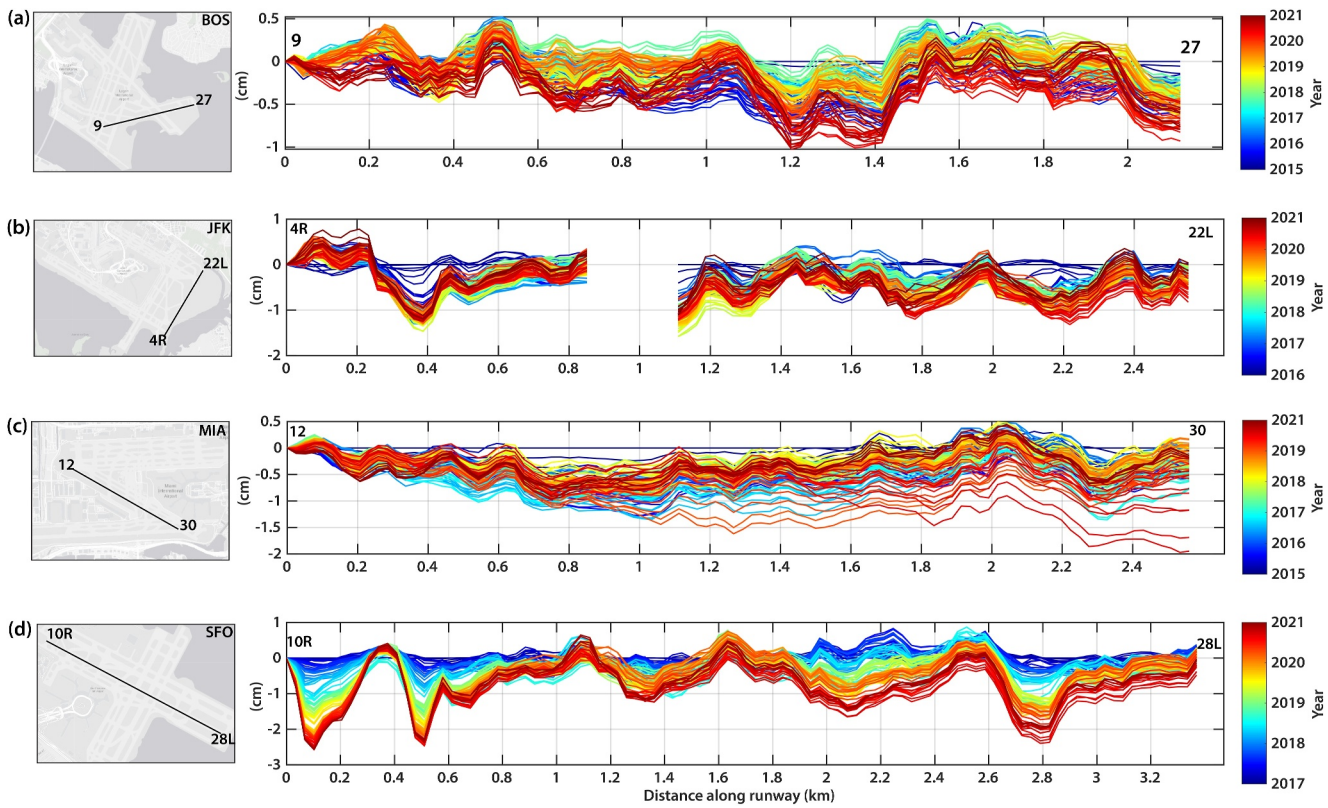

Figure 5. Temporal evolution of vertical displacement along selected airport runways: Each subplot represents a time-series of vertical displacement measurements along key runways at four major U.S. airports: (a) BOS–Runway 9/27 (b) JFK–Runway 4R/22L (c) MIA–Runway 12/30 (d) SFO–Runway 10R/28L. These plots show how surface elevation has changed over time from 2015 to 2021, with displacement values (cm) plotted against the distance along the runway (km). All profiles are referenced to the starting point of 0 km distance. Locations of profiles are shown in the left-side panels. See Figure S4–S18 in Supporting Information S1, for all runway profiles.

decreases over time. The color scale in Figure 6 indicates the magnitude of acceleration, ranging from red (acceleration) to blue (deceleration). Black "X" markers on each airport map, denoting "Critical Areas" where the subsidence rate is greater than 3 mm/yr and acceleration greater than 1 mm/yr^2, suggesting an increasing risk of infrastructure damage.

At the Northeast Corridor, the runways at BOS (Figure 6a) exhibit varying degrees of acceleration. Subsiding pixels, particularly along 15L-33R runway, exhibit an increasing subsidence rate with no critical areas identified. In Figure 6b, DCA shows relatively stable conditions across its runways, except at the intersection of 15–33 and 1–19. No critical areas were marked and acceleration values remained within the green-to-yellow range, suggesting a uniform or decreasing subsidence rate. In contrast, EWR (Figure 6c) shows critical area along runway 11–29, where significant acceleration is incident on high subsidence rates, indicating a rapid increase in deformation over time. The other two runways (4L-22R and 4R-22L) show mixed acceleration and deceleration patterns without a critical area. JFK (Figure 6e) has several critical areas concentrated along segments of runways 13L-31R,13R-31L, and 4R-22L, which exhibit both high subsidence rates and significant acceleration, highlighting localized zones of concern. In Figure 6g, LGA exhibits varying acceleration along its runways (4–22 and 13–31), with no critical areas identified. Lastly, PHL (Figure 6k) shows critical areas along runways 9R-27L and 8–26, where high subsidence rates is compounded by accelerating deformation.

In Southeast airports, MIA (Figure 6i) exhibits several critical areas concentrated along its east-west trending runways (8L-26R and 8R-26L). These zones are characterized by high subsidence rates and significant acceleration, indicating worsening subsidence conditions. In contrast, FLL (Figure 6d), MCO (Figure 6h) and TPA (Figure 6o) show no critical points though there are indications of rapidly increasing subsidence rates along their runways.

10.1029/2025EA004433

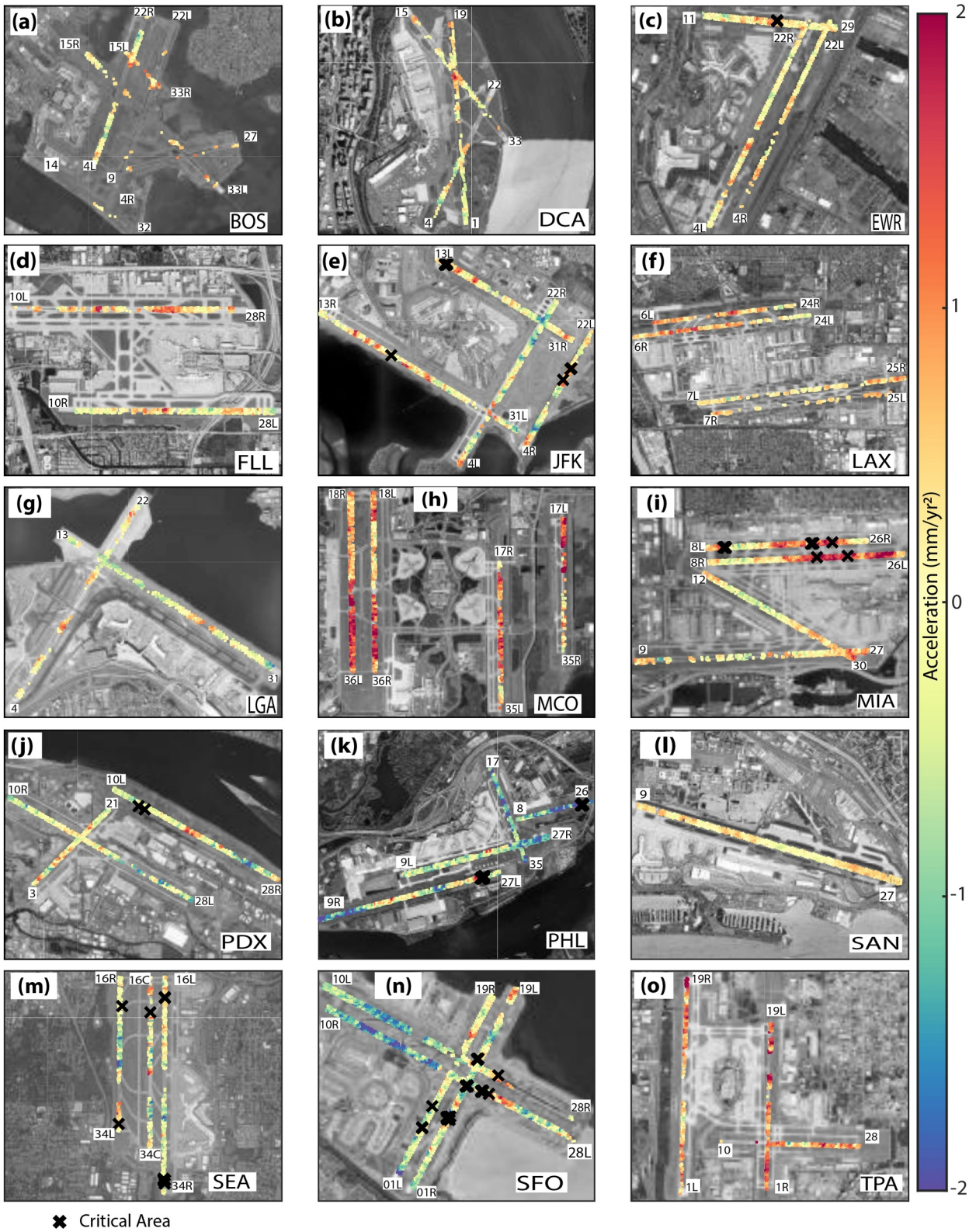

Figure 6. Acceleration rates at subsiding regions along runways at major U.S. airports. The color scale represents acceleration rates in mm/yr^2, ranging from −2 mm/year^2 (blue) to +2 mm/year^2 (red). Black "X" markers indicate critical areas where subsidence rate is greater than 3 mm/yr and the acceleration rate is greater than 1 mm/yr, indicating worsening subsidence. Each airport panels (a–o) includes runway labels and a grayscale ESRI satellite image for geographic reference.

Along the West Coast, SFO (Figure 6n) exhibits multiple critical areas distributed across all four runways (1L-19R, 1R-19L, 10L-28R, and 10R-28L). These zones are primarily concentrated near runway intersections and midpoints. The accelerating deformation at these locations reflects the challenges that SFO's construction on compressible Young Bay Mud poses. In Figure 6j, PDX shows critical areas along runway 10L-28R, particularly toward the 10L ends. The accelerating deformation suggests localized subsurface instability, likely driven by secondary consolidation processes, within underlying clay-rich strata. Similarly, SEA exhibits critical areas along all three runways (Figure 6m), where accelerating deformation affects areas of moderate subsidence rates. In contrast, LAX and SAN do not display critical areas along their runways (Figures 6f and 6l). While most sections of the runways exhibit moderate acceleration, regions of high acceleration do not coincide with high subsidence rates. LAX, in particular, maintains stable conditions across all four parallel runways (6L-24R, 6R-24L, 7L-25R, and 7R-25L), with no critical areas identified, consistent with its low overall subsidence rates.

The accelerating subsidence rates may be attributed to a combination of creep deformation, organic matter decomposition, infrastructure-induced stress redistribution, and groundwater fluctuations (Table 2), collectively indicating a coupled geotechnical–hydrological mechanism affecting runway stability. This accelerating subsidence rates can increase maintenance costs and reduce service lifespans of critical infrastructure by compromising structural integrity. The accelerated subsidence can exacerbate flood risk by lowering land elevation and impairing drainage systems. It can also disrupt underground utilities, including water, sewage, and gas lines, creating safety hazards and service interruptions. The cumulative effect of these impacts strains public resources and highlights the urgent need for proactive monitoring and mitigation strategies.

3.4. Runway Damage Risk Assessment

The structural integrity of airport runways depends not just on the magnitude of VLM, but critically on its spatial gradient. To assess potential damage from differential settlement, we computed angular distortion (β, in μrad/year) between adjacent points along each runway. Angular distortion is a well-established indicator of infrastructure vulnerability, particularly for long, rigid structures like runways, where non-uniform subsidence can lead to slope changes, cracking, ponding, and reduced friction. Figure S3 in Supporting Information S1 provides high-resolution spatial maps of the distortion angle across all monitored runways. Notably, elevated β values—especially those exceeding 20 μrad/year—signal potential operational concerns, as these are associated with significant angular deformation that may not be visible in average VLM trends. Spatial heterogeneity in β could be influenced not only by geology, but also localized variations such as fill material heterogeneity and thickness variations; moisture retention and drainage behavior; historical construction phasing and resurfacing inconsistencies; and aircraft loading patterns and structural response.

The risk of damage along the runways was then inferred from the angular distortions as described in the method section. Figure 7 shows the estimated risk along the runways classified as low (L), medium (M), high (H), and VH. JFK and LAX airports (Figures 7e and 7f), with the highest passenger traffic and aircraft operations in 2024, exhibit runway damage risks primarily in the low to medium range, suggesting these airports maintain relatively stable runway conditions despite their high operational demands. Similarly, BOS, EWR, LGA, MIA and SAN (Figures 7a, 7c, 7g, 7i, and 7l) also show risks restricted to low and medium levels. Several airports, including FLL, PDX, PHL and SFO (Figures 7d, 7j, 7k, and 7n), show an extended range of risks spanning from low to high. This variability indicates localized vulnerabilities in runway segments that may require targeted monitoring and maintenance to prevent operational disruptions. Notably, DCA, MCO, SEA and TPA (Figures 7b, 7h, 7m, and 7o) exhibit the full spectrum of risks, ranging from low to VH. This suggests potential runway damage in specific areas, potentially posing significant operational challenges.

In summary, the percentage of the total area across the 15 airports at low risk is about 96.1%, while the medium, high, and VH are 3.6%, 0.2%, and 0.04% of the total runway areas (Figure 7p).

4. Discussion

This study presents the first high-resolution map of VLM at 15 major U.S. airports using an analysis of Sentinel-1 radar data, revealing spatially heterogeneous subsidence patterns with significant implications for infrastructure vulnerabilities and resilience. Our validation against GNSS measurements demonstrates the reliability of InSAR-

Table 2
Drivers of Land Subsidence at Each Airport

Airport	Geology	Primary causes of land subsidence	Reference
Logan International Airport (BOS)	Artificial fill over Boston Blue Clay, glacial till, and bedrock	GIA, groundwater extraction, urban load-induced subsidence	(Baise et al., 2016; Himick & Schwank, 1997)
Ronald Reagan Washington National Airport (DCA)	Upper stratum of fill material, organic silt stratum, clayey sand interbedded with sandy clay	Riverbank erosion, consolidation of fill material	US Army Corps of Engineers (2023)
Newark Liberty International Airport (EWR)	Saturated estuarine deposits, organic silts and clays over glacial deposits	Aquifer depletion, urban development impact	Weston (1998)
Fort Lauderdale–Hollywood International Airport (FLL)	Sandy fill over limestone and sandstone (Biscayne Aquifer)	Coastal sediment compaction, groundwater pumping	(Fiaschi & Wdowinski, 2020; Randazzo & Smith, 2003; Wdowinski et al., 2020)
John F. Kennedy International Airport (JFK)	Sandy fill over organic marsh deposits and glacial outwash	Glacial isostatic adjustment (GIA), soil compression	Horvath (2014)
Los Angeles International Airport (LAX)	Alluvial sediments over marine terrace deposits	Groundwater/hydrocarbon extraction, soil compaction	(Hu et al., 2019; Khorrami et al., 2023)
LaGuardia Airport (LGA)	Hydraulic fill over organic marine deposits and glacial till	GIA, soil compaction	(Buzzanga et al., 2023; Mikolic et al., 2013)
Orlando International Airport (MCO)	Quaternary sands over limestone (Floridan Aquifer)	Karst terrain, subsurface erosion	Randazzo and Smith (2003)
Miami International Airport (MIA)	Miami Limestone overlain by sandy soils and artificial fill	Karst geology, sediment compaction, soil oxidation, and sinkhole activity.	(Fiaschi & Wdowinski, 2020; Randazzo & Smith, 2003; Wdowinski et al., 2020)
Portland International Airport (PDX)	Artificial fill over alluvial deposits, compressible silts and clays	Volcanic soil compaction, tectonic activity	Multi-Hazard Mitigation Council (2021)
Philadelphia International Airport (PHL)	alluvial deposits, marsh sediments, and artificial fill over impervious clay layer	Urban development, groundwater depletion	Federal Aviation Administration (1994)
San Diego International Airport (SAN)	Artificial fill over marine bay deposits and alluvial sediments	Seismic activity, coastal erosion, artificial fill	Vrugt et al. (1996)
Seattle–Tacoma International Airport (SEA)	Glacial deposits (till and outwash) over bedrock	Soft soil consolidation, tectonic activity	(Galster & Laprade, 1991; Newton et al., 2021)
San Francisco International Airport (SFO)	Hydraulic fill over Young Bay Mud (compressible marine clay)	Soil compaction in reclaimed land, seismic activity	(Blackwell et al., 2020; Bürgmann et al., 2006)
Tampa International Airport (TPA)	Sandy soils over limestone (Floridan Aquifer)	Coastal processes, organic soil compression	Seltzer et al. (2020)

derived VLM estimates, establishing this methodology as a practical approach for monitoring critical transportation infrastructure.

4.1. Regional Subsidence Characteristics and Drivers

4.1.1. Northeast Corridor Airports: Complex Deformation Patterns

The Northeast Corridor airports demonstrate complex patterns of alternating uplift and subsidence, reflecting variable geological foundations, including glacial deposits, coastal fill, and reclaimed wetlands. JFK has the largest total subsiding runway area (465,300 m^2), partly influenced by GIA affecting the region (Buzzanga et al., 2023; Karegar et al., 2016; Ohenhen et al., 2023). JFK exhibits high subsidence acceleration, with critical

10.1029/2025EA004433

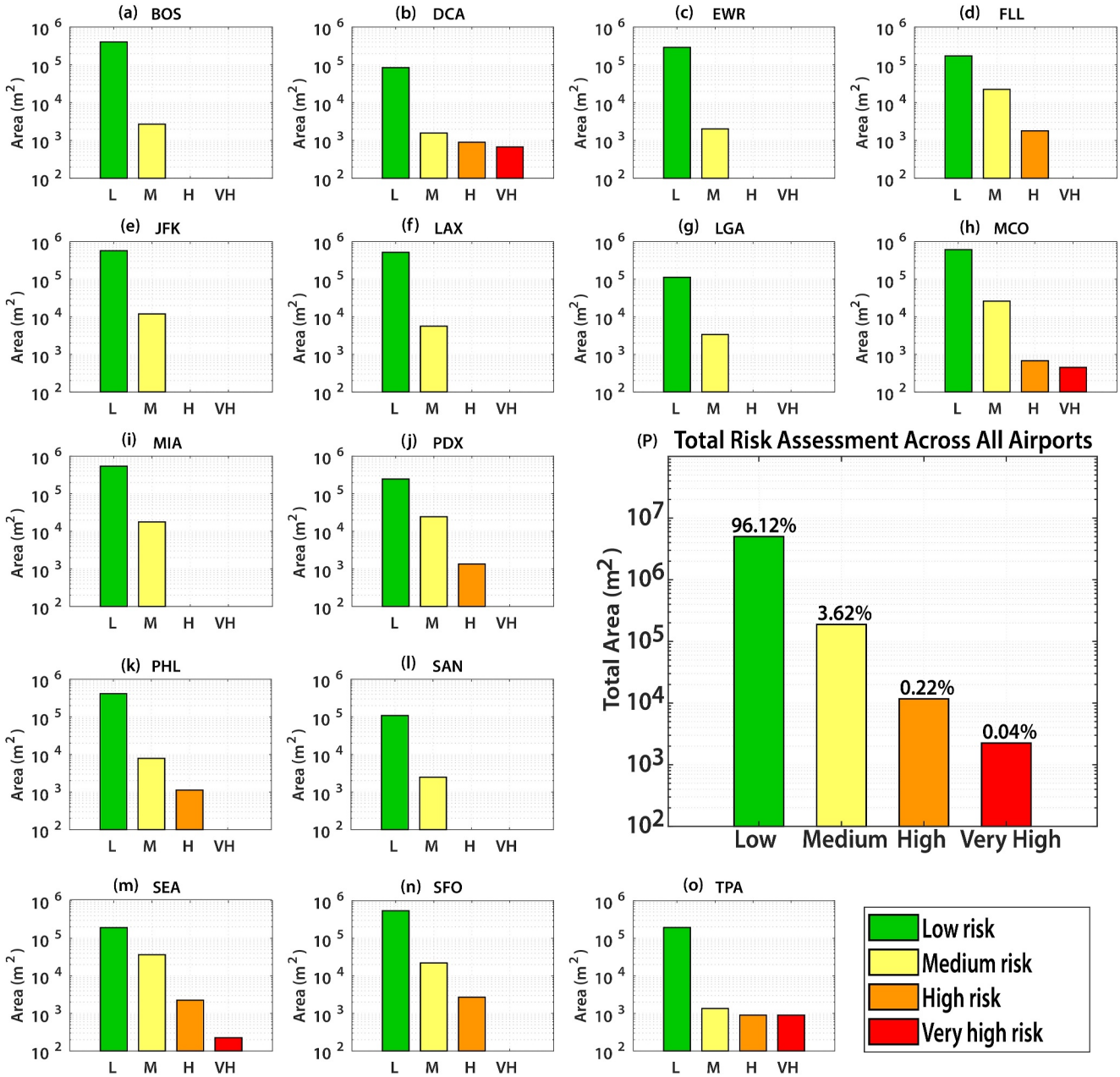

Figure 7. Potential Risk Assessment of Differential Subsidence Impacts at Major U.S. Airports. This figure presents the risk classification of subsidence impact areas across 15 major U.S. airports, categorized into four risk levels: Low (L, green), Medium (M, yellow), High (H, orange), and Very-High (VH, red). Each subfigure (a–o) represents an individual airport, while panel (p) provides an aggregate risk assessment across all airports. Note that vertical axis is presented in logarithmic scale.

areas identified along runways 13L-31R, 13R-31L, and 4R-22L, highlighting risks of long-term runway settlement and structural instability.

EWR demonstrates how local geological variations create differential settlement within a single facility. The concentrated subsidence along runway 11–29, particularly at the northwestern end (-4.2 ± 0.2 mm/yr), corresponds to areas constructed on former wetlands with thick deposits of highly compressible organic soils. This pattern mirrors findings from studies of coastal infrastructure built on reclaimed wetlands, where post-construction settlement can persist for decades (Kumamoto et al., 2017; Wang et al., 2016; Zhuo et al., 2020).

The variable subsidence rates across EWR's three runways illustrate how construction age and techniques influence settlement patterns, with newer sections potentially benefiting from improved foundation designs.

In contrast, BOS, LGA, and DCA airports exhibit more stable conditions, with localized acceleration in some runway segments but no widespread critical areas. DCA has the lowest total subsiding runway area (77,625 m^2) among Northeast airports. The presence of uplifts in some regions suggests localized geotechnical stability measures, although variable motion may introduce differential settlement risks in the future.

4.1.2. Southeast Airports: Karst-Influenced Subsidence

Subsidence dynamics across Southeast airports reveal site-specific vulnerabilities driven by complex interactions between geology, soil properties, and hydrological processes (Fiaschi & Wdowinski, 2020). At MIA, deformation is both spatially extensive and locally intensified, with critical acceleration zones indicating ongoing subsurface instability. The peak subsidence rate of -4.0 ± 0.1 mm/yr and area-weighted average of -1.0 mm/yr suggest persistent ground movement that may compromise long-term runway performance. FLL exhibits moderate and spatially variable subsidence, with acceleration localized along specific runways—particularly 28L and 10R-28L—where patterns of differential settlement may signal evolving structural stress. TPA, while not exhibiting sharply defined critical zones, shows a consistent trend of acceleration across all runways, pointing to a gradual but widespread increase in subsidence rates that warrant long-term monitoring. In contrast, MCO maintains relatively stable ground conditions with no significant deformation patterns detected, highlighting the variability of subsidence risk even within geologically similar regions. Collectively, these patterns emphasize the need for continuous, high-resolution monitoring to detect early signs of infrastructure stress and inform proactive mitigation strategies.

4.1.3. West Coast Airports: Critical Subsidence Hotspots

West Coast airports exhibit the most severe subsidence patterns nationally, with geological settings serving as the primary determinant of stability. SFO demonstrates the highest area-weighted subsidence rate (-2.4 mm/yr) and most extreme localized deformation (-9.2 ± 0.2 mm/yr). This significant subsidence is driven by the compressible Young Bay Mud underlying much of the airport, aligning with previous studies documenting regional subsidence related to natural sediment compaction and historical groundwater extraction (Blackwell et al., 2020; Shirzaei & Bürgmann, 2018). The accelerating deformation at SFO is concentrated along all four runways, primarily at runway intersections and midpoints, exacerbating infrastructure vulnerabilities and is particularly concerning given the airport's low elevation and proximity to San Francisco Bay.

PDX and SEA airports also exhibit significant subsidence with distinctive acceleration patterns. The presence of multiple localized critical areas suggests underlying geophysical processes such as soil consolidation and hydrological changes influencing subsidence acceleration, highlighting the gradual deterioration of infrastructure stability in these regions. Portland's location in the Columbia River floodplain, with its heterogeneous alluvial deposits and history of artificial fill placement, creates complex foundation conditions manifesting in variable subsidence patterns. The maximum subsidence rate of -6.8 ± 0.2 mm/yr at PDX represents a significant infrastructure concern, particularly given the airport's seismic vulnerability in the Cascadia region.

In contrast, LAX and SAN airports exhibit relatively stable conditions, with low subsidence rates and no critical acceleration areas. LAX, in particular, benefits from its geological setting on alluvial sediments, providing greater structural stability than the reclaimed or organic-rich deposits underlying other West Coast airports.

4.2. Infrastructure Implications and Risk Assessment

4.2.1. Differential Settlement and Infrastructure Damage Risk

The displacement gradient analysis revealed varying levels of surface distortion and runway damage risk across the studied airports. Most airports exhibited predominantly low risk, except for DCA, MCO, SEA, and TPA, which have localized zones of high to VH risk. With over $100 billion in estimated nationwide airport infrastructure needs (Airports Council International, 2023), we recommend that runways exposed to high damage risks should be prioritized for the $62.4 billion available in Airport Improvement Program and Bipartisan Infrastructure Law funding through 2,027 (Federal Aviation Administration, 2023). Timely identification, maintenance, and rehabilitation of high-risk runways will enhance safety, prevent further deterioration, and reduce long-term costs.

4.2.2. Compound Climate Vulnerabilities

Beyond structural damage from differential subsidence, coastal airports face compound vulnerabilities from sea level rise and storm surges (International Civil Aviation Organization (ICAO), 2020). Eight airports in this study —LGA, JFK, DCA, LAX, MIA, SAN, SFO, and TPA—are in low elevation coastal zones (<10 m amsl). Ongoing subsidence at these locations will exacerbate flood risk and further strain infrastructure resilience. Climate change-induced soil instability, natural compaction, and aquifer depletion significantly contribute to VLM, as observed across individual airports, further exacerbating runway subsidence and infrastructure vulnerabilities. Proactive investment will be required to flood-proof these vulnerable airports to withstand future disasters and reduce costly damage repairs.

4.2.3. Applications and Future Directions

This study demonstrates the operational value of high-resolution Earth observation satellite data and InSAR techniques for routine monitoring of subsidence and risk assessment along airport runways. This methodology is applicable to various infrastructure types, including roads, bridges, levees, and buildings, for monitoring potential subsidence-induced damage. Integration with instrumented sensors could enable advanced early warning and risk-based safety management systems that alert officials when differential subsidence thresholds are exceeded, enhancing infrastructure resilience against land deformation.

Implementation of this approach aligns with United Nations Sustainable Development Goals (SDGs), particularly SDG 9 (Industry, Innovation, and Infrastructure) and SDG 11 (Sustainable Cities and Communities). Numerous global aviation hubs in sinking coastal and deltaic regions—including Changi Airport in Singapore, Schiphol Airport in the Netherlands, and Kansai International Airport in Japan—would benefit from integrating InSAR-based monitoring with existing risk management frameworks to enhance long-term infrastructure resilience in the face of increasing climate-related challenges.

4.2.4. Smart Infrastructure Monitoring With Satellite Remote Sensing

To strengthen infrastructure resilience and adapt to and mitigate the impact of natural hazards, we propose a framework that leverages satellite remote sensing, ground-based sensors, and advanced analytics (Figure 8). This framework relies on satellite remote sensing to collect high-resolution spatial data on infrastructure deformation, land subsidence, surface water changes, and other environmental conditions. It also uses ground-based sensors to provide complementary, real-time measurements such as structural vibration, temperature, and ground displacement. The data from multiple sources are then aggregated and synchronized for real-time analysis and long-term trend assessment. Artificial intelligence powered analytics detect patterns, forecast risks, and generate insights to support adaptation, mitigation, and resilience planning. Finally, the user interface offers infrastructure managers and stakeholders dashboards, alerts, and reports through mobile and desktop platforms.

As visualized in Figure 8, the satellite data is critical in identifying high-risk areas where targeted investments can mitigate vulnerabilities, such as preventing land subsidence through managed aquifer recharge. Near real-time monitoring further empowers infrastructure operators to implement proactive adaptation measures, such as structural reinforcements or operational adjustments, to address emerging risks. Predictive models offer valuable insights into maintaining infrastructure functionality under the combined pressures of climate change and human activities, minimizing downtime and reducing long-term costs. The proposed framework is versatile and applicable to various infrastructure types—such as bridges, railways, ports, urban areas, and water and energy systems —across diverse geographic regions. Its key strength lies in its holistic approach, integrating resilience, adaptation, and mitigation strategies. Depending on specific conditions, the framework recommends tailored solutions, such as strengthening infrastructure to withstand shocks (e.g., extreme weather, earthquakes, or subsidence), redesigning infrastructure and maintenance plans to adapt to evolving environmental conditions or implementing strategies to reduce long-term risks and environmental impacts. This comprehensive approach ensures sustainable and resilient infrastructure systems in the face of growing challenges.

The proposed framework delivers significant outcomes and benefits, including improved infrastructure resilience through near real-time monitoring, which prevents catastrophic failures and extends the lifespan of critical infrastructure. It enables cost-effective maintenance by prioritizing activities based on data-driven insights, reducing unnecessary expenditures, and optimizing resource allocation. Additionally, the framework enhances

10.1029/2025EA004433

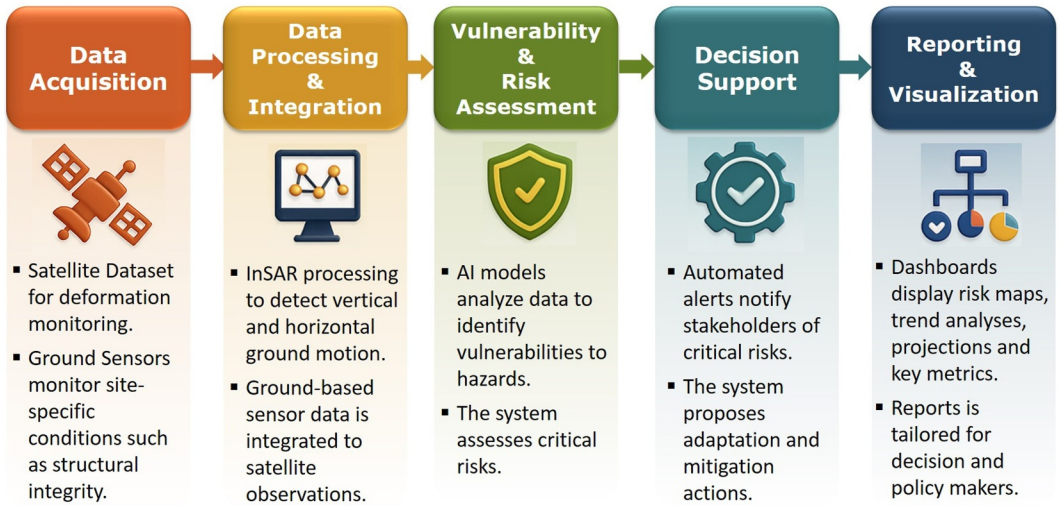

Figure 8. Framework for a smart infrastructure monitoring system relying on satellite remote sensing. This framework integrates satellite remote sensing technologies, particularly interferometric synthetic aperture radar, with data analytics and ground-based systems to monitor and manage infrastructure in real time.

adaptation capacity by enabling early detection of environmental risks, allowing timely responses to climate change, and minimizing long-term impacts. Finally, it supports sustainable development by guiding infrastructure investments through comprehensive risk assessments, promoting both economic stability and environmental sustainability.

5. Conclusions

This study demonstrates the effectiveness of InSAR for high-resolution monitoring of VLM at major U.S. airports, providing a systematic framework for identifying subsidence-related risks to runway infrastructure. Using Sentinel-1 SAR data, we analyzed 15 major U.S. airports, revealing significant spatiotemporal variations in subsidence rates, with SFO experiencing the highest rate (-9.2 ± 0.2 mm/yr) and LAX showing the lowest rate (-2.0 ± 0.2 mm/yr).

Our results indicate that 96.1% of total runway areas fall under low-risk categories, but 3.6%, 0.2%, and 0.04% of airport infrastructure are classified as medium, high, and VH risk, respectively. Approximately 3.5 million m^2 of runways are exposed to subsidence rates exceeding 5 mm/year, with 13,950 m^2 classified as high to VH damage risk zones. This differential subsidence poses serious challenges, potentially leading to runway slope changes, cracking, drainage issues, and compromised operational safety for airport facilities.

Comparisons between InSAR-derived subsidence estimates and GNSS data confirm the robustness of our approach, with R^2 of 0.81, demonstrating the reliability of satellite-based infrastructure monitoring. Furthermore, the analysis of the mean acceleration and angular distortion along runways enabled us to identify critical areas and categorize risk levels, identifying locations where subsidence-induced deformation could lead to structural damage and operational hazards.

These findings highlight the urgent need for targeted infrastructure investments, proactive monitoring strategies, and adaptive management plans to mitigate the risks associated with subsidence at U.S. airports. Given the increasing vulnerability of coastal airports due to sea level rise, storm surges, and land subsidence, integrating high-resolution InSAR monitoring into routine airport maintenance protocols can provide early warnings of deformation-related risks before they impact aviation safety and efficiency.

Conflict of Interest

The authors declare no conflicts of interest relevant to this study.

Data Availability Statement

SAR data sets are available at the Alaska satellite facilities at https://vertex.daac.asf.alaska.edu/. GNSS velocities information is obtained from the Nevada Geodetic lab (http://geodesy.unr.edu/magnet.php). The SAR analysis was performed using the WabInSAR algorithm, version 5.6, which is available at https://www.eoivt.com/software. The VLM rates and their associated standard deviation data sets (Dasho & Shirzaei, 2025) referenced in this manuscript are publicly available via the Virginia Tech Data Repository at https://doi.org/10.7294/29114843.

Acknowledgments
This work was supported by grants from NASA (16-SLCT16-0008) and the Department of Defense, which supported the contributions of O.D. and M.S. We thank the editor and reviewers for their valuable comments and constructive suggestions.

References

Abidin, H. Z., Andreas, H., Gumilar, I., & Brinkman, J. J. (2015). Study on the risk and impacts of land subsidence in Jakarta. *Proceedings of the International Association of Hydrological Sciences*, *372*, 115–120. https://doi.org/10.5194/piahs-372-115-2015

Airports Council International. (2023). 2023 US airport infrastructure needs report. Retrieved from https://airportscouncil.org/wp-content/uploads/2023/03/2023ACI-NAInfrastructureNeedsReportFINAL.pdf

Albano, M., Chiaradonna, A., Saroli, M., Moro, M., Pepe, A., & Solaro, G. (2024). InSAR analysis of post-liquefaction consolidation subsidence after 2012 Emilia earthquake sequence (Italy). *Remote Sensing*, *16*(13), 2364. https://doi.org/10.3390/rs16132364

An, B., Jiang, Y., Wang, C., Shen, P., Song, T., Hu, C., & Liu, K. (2023). Ground infrastructure monitoring in coastal areas using time-series InSAR technology: The case study of Pudong international airport, Shanghai. *International Journal of Digital Earth*, *16*(1), 355–374. https://doi.org/10.1080/17538947.2023.2171144

Baise, L. G., Kaklamanos, J., Berry, B. M., & Thompson, E. M. (2016). Soil amplification with a strong impedance contrast: Boston, Massachusetts. *Engineering Geology*, *202*, 1–13. https://doi.org/10.1016/j.enggeo.2015.12.016

Blackwell, E., Shirzaei, M., Ojha, C., & Werth, S. (2020). Tracking California's sinking coast from space: Implications for relative sea-level rise. *Science Advances*, *6*(31), 1–10. https://doi.org/10.1126/sciadv.aba4551

Blewitt, G., Kreemer, C., Hammond, W. C., & Gazeaux, J. (2016). MIDAS robust trend estimator for accurate GPS station velocities without step detection. *Journal of Geophysical Research: Solid Earth*, *121*(3), 2054–2068. https://doi.org/10.1002/2015JB012552

Bürgmann, R., Hilley, G., Ferretti, A., & Novali, F. (2006). Resolving vertical tectonics in the San Francisco Bay area from permanent scatterer InSAR and GPS analysis. *Geology*, *34*(3), 221–224. https://doi.org/10.1130/G22064.1

Burland, J. B., & Wroth, C. (1975). *Settlement of buildings and associated damage*. Building Research Establishment.

Buzzanga, B., Bekaert, D. P. S., Hamlington, B. D., Kopp, R. E., Govorcin, M., & Miller, K. G. (2023). Localized uplift, widespread subsidence, and implications for sea level rise in the New York city metropolitan area. *Science Advances*, *9*(39), 7–12. https://doi.org/10.1126/sciadv.adi8259

Cavalié, O., Sladen, A., & Kelner, M. (2015). Detailed quantification of delta subsidence, compaction and interaction with man-made structures: The case of the NCA airport, France. *Natural Hazards and Earth System Sciences*, *15*(9), 1973–1984. https://doi.org/10.5194/nhess-15-1973-2015

Ciampoli, L. B., Gagliardi, V., Ferrante, C., Calvi, A., D'amico, F., & Tosti, F. (2020). Displacement monitoring in airport runways by persistent scatterers sar interferometry. *Remote Sensing*, *12*(21), 1–14. https://doi.org/10.3390/rs12213564

Cigna, F., & Tapete, D. (2021). Present-day land subsidence rates, surface faulting hazard and risk in Mexico City with 2014–2020 Sentinel-1 IW InSAR. *Remote Sensing of Environment*, *253*, 112161. https://doi.org/10.1016/j.rse.2020.112161

Costantini, M., & Rosen, P. A. (1999). Generalized phase unwrapping approach for sparse data. *International Geoscience and Remote Sensing Symposium (IGARSS)*, *1*, 267–269. https://doi.org/10.1109/igarss.1999.773467

Dai, K., Shi, X., Gou, J., Hu, L., Chen, M., Zhao, L., et al. (2020). Diagnosing subsidence geohazard at Beijing capital international airport, from high-resolution SAR interferometry. *Sustainability*, *12*(6), 1–16. https://doi.org/10.3390/su12062269

Dasho, O., & Shirzaei, M. (2025). Sinking airports: A glance at the State of US transport infrastructure [Dataset]. *University Libraries, Virginia Tech*. https://doi.org/10.7294/29114843

Davydzenka, T., Tahmasebi, P., & Shokri, N. (2024). Unveiling the global extent of land subsidence: The sinking crisis. *Geophysical Research Letters*, *51*(4), e2023GL104497. https://doi.org/10.1029/2023GL104497

Day, R. W. (1990). Differential movement of slab-on-grade structures. *Journal of Performance of Constructed Facilities*, *4*(4), 236–241. https://doi.org/10.1061/(asce)0887-3828(1990)4:4(236)

Farr, T. G., Rosen, P. A., Caro, E., Crippen, R., Duren, R., Hensley, S., et al. (2007). The shuttle radar topography mission. *Reviews of Geophysics*, *45*(2), 1–13. https://doi.org/10.1029/2005rg000183

Federal Aviation Administration. (1994). Finding of no significant impact (PHL). Retrieved from https://www.phl.org/drupalbin/media/runway8-261994.pdf

Federal Aviation Administration (FAA). (2023). National plan of integrated airport systems (NPIAS) 2023–2027 (Vol. *90*). Retrieved from https://www.faa.gov/sites/faa.gov/files/npias-2023-2027-narrative.pdf

Fergason, K. C., Rucker, M. L., & Panda, B. B. (2015). Methods for monitoring land subsidence and earth fissures in the Western USA. *Proceedings of the International Association of Hydrological Sciences*, *372*, 361–366. https://doi.org/10.5194/piahs-372-361-2015

Fernaoóndez-Torres, E., Cabral-Cano, E., Solano-Rojas, D., Havazli, E., & Salazar-Tlaczani, L. (2020). Land subsidence risk maps and InSAR based angular distortion structural vulnerability assessment: An example in Mexico City. *Proceedings of the International Association of Hydrological Sciences*, *382*, 583–587. https://doi.org/10.5194/piahs-382-583-2020

Fiaschi, S., & Wdowinski, S. (2020). Local land subsidence in Miami beach (FL) and Norfolk (VA) and its contribution to flooding hazard in coastal communities along the U.S. Atlantic coast. *Ocean & Coastal Management*, *187*, 105078. https://doi.org/10.1016/j.ocecoaman.2019.105078

Franceschetti, G., & Lanari, R. (1999). Synthetic aperture radar processing, CRC press. *Electronic Engineering Systems Series*.

Gagliardi, V., Bianchini Ciampoli, L., Trevisani, S., D'amico, F., Alani, A. M., Benedetto, A., & Tosti, F. (2021). Testing sentinel-1 sar interferometry data for airport runway monitoring: A geostatistical analysis. *Sensors*, *21*(17), 5769. https://doi.org/10.3390/s21175769

Galloway, D. L., Jones, D. R., & Ingebritsen, S. E. (2000). Measuring land subsidence from space. GS fact Sheet-051-00, April (Vol. *1–4*). Retrieved from https://pubs.usgs.gov/fs/fs-051-00/pdf/fs-051-00.pdf

Galster, R. W., & Laprade, W. T. (1991). Geology of Seattle, Washington, United States of America. *Environmental and Engineering Geoscience*, *xxviii*(3), 235–302. https://doi.org/10.2113/gseegeosci.xxviii.3.235

Gao, M., Gong, H., Li, X., Chen, B., Zhou, C., Shi, M., et al. (2019). Land subsidence and ground fissures in Beijing capital international airport (BCIA): Evidence from Quasi-PS InSAR analysis. *Remote Sensing*, *11*(12), 1466. https://doi.org/10.3390/rs11121466

Gerardi, T. (2007). The impact of runway roughness in a high speed aborted takeoff. In *FAA worldwide airport technology transfer conference* (Vol. 4). Retrieved from https://www.airporttech.tc.faa.gov/Collaboration/Past-Conferences-Events/Airport-Technology-Transfer-Conference-2007/the-impact-of-runway-roughness-during-a-high-speed-aborted-takeoff

Hammond, W. C., Blewitt, G., Kreemer, C., & Nerem, R. S. (2021). GPS imaging of global vertical land motion for studies of sea level rise. *Journal of Geophysical Research: Solid Earth*, *126*(7), e2021JB022355. https://doi.org/10.1029/2021JB022355

Himick, D. E., & Schwank, S. (1997). Central Artery/Tunnel project (CA/T) in Boston, Massachusetts, USA: Construction of diaphragm walls under limited headroom. In *14th international conference on soil mechanics and foundation engineering* (Vol. 4, pp. 1407–1410). Retrieved from https://www.issmge.org/uploads/publications/1/31/1997_03_0005.pdf

Horvath, J. S. (2014). John F. Kennedy International airport: A seven-decade case study of the evolution of geotechnical and foundation engineering design and construction practice. (Issue November). Retrieved from http://www.pilelineonline.com/pdfs/2014-4_jshce-wp_JFKIA_Rev1.pdf

Hu, B., Chen, X., & Zhang, X. (2019). Using multisensor SAR datasets to monitor land subsidence in Los Angeles from 2003 to 2017. *Journal of Sensors*, 9389820. https://doi.org/10.1155/2019/9389820

Huseby, A. B., & Rabbe, M. (2018). Optimizing warnings for slippery runways based on weather data. In *Safety and reliability–Safe societies in a changing world–Proceedings of the 28th international European safety and reliability conference* (Vol. 2018, pp. 2789–2796). ESREL. https://doi.org/10.1201/9781351174664-350

International Civil Aviation Organization (ICAO). (2020). Eco-Airport Tool Kit: Climate resilient airports. Retrieved from https://www2023.icao.int/environmental-protection/Documents/Climate%20resilient%20airports.pdf

Jiang, L., Zhao, Q., Cheng, S., & Lin, H. (2008). Integrated analysis of PSInSAR and geological data for investigating local differential settlement of new Hong Kong international airport. *International Conference on Earth Observation Data Processing and Analysis (ICEODPA)*, *7285*, 72854D. https://doi.org/10.1117/12.815936

Karegar, M. A., Dixon, T. H., & Engelhart, S. E. (2016). Subsidence along the Atlantic Coast of North America: Insights from GPS and late Holocene relative sea level data. *Geophysical Research Letters*, *43*(7), 3126–3133. https://doi.org/10.1002/2016GL068015

Khorrami, M., Shirzaei, M., Ghobadi-Far, K., Werth, S., Carlson, G., & Zhai, G. (2023). Groundwater volume loss in Mexico City constrained by InSAR and GRACE observations and mechanical models. *Geophysical Research Letters*, *50*(5), 1–11. https://doi.org/10.1029/2022gl101962

Kumamoto, N., Tsuchida, T., Fukuhara, K., & Kitayama, N. (2017). Study on long-term settlement behavior of reclaimed land based on the observed data in Hiroshima Bay. *Japanese Geotechnical Journal*, *12*(1), 65–78. https://doi.org/10.3208/jgs.12.65

Lee, J. C., & Shirzaei, M. (2023). Novel algorithms for pair and pixel selection and atmospheric error correction in multitemporal InSAR. *Remote Sensing of Environment*, *286*, 113447. https://doi.org/10.1016/j.rse.2022.113447

Lenardón Sánchez, M., Farías, C. A., & Cigna, F. (2024). Multi-decadal land subsidence risk assessment at major Italian cities by integrating PSInSAR with urban vulnerability. *Land*, *13*(12), 2103. https://doi.org/10.3390/land13122103

Li, M., Chen, J.-J., Xu, Y., Tong, D., Cao, W., & Shi, Y.-J. (2021). Effects of groundwater exploitation and recharge on land subsidence and infrastructure settlement patterns in shanghai. *Engineering Geology*, *282*, 105995. https://doi.org/10.1016/J.ENGGEO.2021.105995

Mario Costantini, T. (1998). A novel phase unwrapping method based on network programming. *IEEE Transactions on Geoscience and Remote Sensing*, *36*(3), 813–821. https://doi.org/10.1109/36.673674

Mehta, Y., Cleary, D., & Ali, A. W. (2017). Field cracking performance of airfield rigid pavements. *Journal of Traffic and Transportation Engineering*, *4*(4), 380–387. https://doi.org/10.1016/j.jtte.2017.05.010

Mikhail, E. M., & Ackermann, F. E. (1982). *Observations and least squares*. University Press of America.

Mikolic, F. G., Lawrence, J. W., & Albright, B. M. (2013). Phase IA archaeological survey report: LaGuardia airport central terminal building redevelopment. In *Aecom*. (Issue June). Retrieved from https://s-media.nyc.gov/agencies/lpc/arch_reports/1553.pdf

Miller, M. M., & Shirzaei, M. (2019). Land subsidence in Houston correlated with flooding from Hurricane Harvey. *Remote Sensing of Environment*, *225*, 368–378. https://doi.org/10.1016/j.rse.2019.03.022

Mohseni, N., & Bol, R. (2021). Variation in the rate of land subsidence induced by groundwater extraction and its effect on the response pattern of soil microbial communities. *Earth Surface Processes and Landforms*, *46*(10), 1898–1908. https://doi.org/10.1002/esp.5133

Multi-Hazard Mitigation Council. (2021). PDX resilient runway benefit-cost analysis. Principal Investigator Porter, K., Co-Principal Investigators Rose, A., and Santos, J., Investigator Wei, D., Yuan, J., Director, MMC. *National Institute of Building Sciences*. Retrieved from www.nibs.org

Newton, T., Weldon, R., Miller, I., Schmidt, D., Mauger, G., Morgan, H., & Grossman, E. (2021). An assessment of vertical land movement to support coastal hazards planning in Washington state. *Water*, *13*(3), 281. https://doi.org/10.3390/W13030281

Ohenhen, L. O., & Shirzaei, M. (2022). Land subsidence hazard and building collapse risk in the coastal city of Lagos, West Africa. *Earth's Future*, *10*(12), 1–12. https://doi.org/10.1029/2022EF003219

Ohenhen, L. O., Shirzaei, M., & Barnard, P. L. (2024). Slowly but surely: Exposure of communities and infrastructure to subsidence on the US east coast. *PNAS Nexus*, *3*(1), pgad426. https://doi.org/10.1093/pnasnexus/pgad426

Ohenhen, L. O., Shirzaei, M., Ojha, C., & Kirwan, M. L. (2023). Hidden vulnerability of US Atlantic coast to sea-level rise due to vertical land motion. *Nature Communications*, *14*(1), 2038. https://doi.org/10.1038/s41467-023-37853-7

Randazzo, A. F., & Smith, D. L. (2003). Subsidence-induced foundation failures in Florida's karst terrain. Sinkholes and the engineering and environmental impacts of Karst (pp. 82–94). https://doi.org/10.1061/40698(2003)7

Robson, G., Treitz, P., Lamoureux, S., Murnaghan, K., & Brisco, B. (2021). Seasonal surface subsidence and frost heave detected by C-Band DInSAR in a high arctic environment, cape bounty, Melville Island, Nunavut, Canada. *Remote Sensing*, *13*, 2505. https://doi.org/10.3390/rs13132505

Rouyet, L., Lauknes, T., Christiansen, H., Strand, S., & Larsen, Y. (2019). Seasonal dynamics of a permafrost landscape, Adventdalen, Svalbard, investigated by InSAR. *Remote Sensing of Environment*, *231*, 111236. https://doi.org/10.1016/J.RSE.2019.111236

Sato, H. P., Abe, K., & Ootaki, O. (2003). GPS-measured land subsidence in Ojiya City, Niigata Prefecture, Japan. *Engineering Geology*, *67*(3–4), 379–390. https://doi.org/10.1016/S0013-7952(02)00221-1

Seltzer, J. P., Meyer, M. E., Ortiz, C. H., & Dean, J. A. (2020). Drilled shaft foundation solution at a challenging, variable karst site in Tampa. *GeoCongress*, *2020*, 175–189. https://doi.org/10.1061/9780784482780.017

Shirzaei, M. (2013). A wavelet-based multitemporal DInSAR algorithm for monitoring ground surface motion. *IEEE Geoscience and Remote Sensing Letters*, *10*(3), 456–460. https://doi.org/10.1109/LGRS.2012.2208935

Shirzaei, M., & Bürgmann, R. (2012). Topography correlated atmospheric delay correction in radar interferometry using wavelet transforms. *Geophysical Research Letters*, *39*(1), 1–6. https://doi.org/10.1029/2011GL049971

Shirzaei, M., & Bürgmann, R. (2018). Global climate change and local land subsidence exacerbate inundation risk to the San Francisco Bay area. *Science Advances*, *4*(3), 1–9. https://doi.org/10.1126/sciadv.aap9234

Shirzaei, M., Bürgmann, R., & Fielding, E. J. (2017). Applicability of Sentinel-1 terrain observation by progressive scans multitemporal interferometry for monitoring slow ground motions in the San Francisco Bay area. *Geophysical Research Letters*, *44*(6), 2733–2742. https://doi.org/10.1002/2017GL072663

Skempton, A. W., & MacDonald, D. H. (1956). The allowable settlements of buildings. *Proceedings–Institution of Civil Engineers*, *5*(6), 727–768. https://doi.org/10.1680/ipeds.1956.12202

Smith, R., & Majumdar, S. (2020). Groundwater storage loss associated with land subsidence in Western United States mapped using machine learning. *Water Resources Research*, *56*(7), e2019WR026621. https://doi.org/10.1029/2019WR026621

US Army Corps of Engineers. (2023). Metropolitan Washington District of Columbia coastal storm risk management feasibility study. Appendix D: Geotechnical analysis northern Virginia. (Issue October). Retrieved from https://usace.contentdm.oclc.org/digital/collection/p16021coll7/id/25596

Valman, S., Siewert, M., Boyd, D., Ledger, M., Gee, D., De La Barreda-Bautista, B., et al. (2024). InSAR-measured permafrost degradation of Palsa peatlands in northern Sweden. *The Cryosphere*, *18*(4), 1773–1790. https://doi.org/10.5194/tc-18-1773-2024

van de Vrugt, H., Day, S., Magistrale, H., & Weddberg, J. (1996). Inversion of local earthquake data for site response in San Diego, California. *Bulletin of the Seismological Society of America*, *86*(5), 1447–1458. https://doi.org/10.1785/BSSA0860051447

Vassileva, M., Al-Halbouni, D., Motagh, M., Walter, T. R., Dahm, T., & Wetzel, H. U. (2021). A decade-long silent ground subsidence hazard culminating in a metropolitan disaster in Maceió, Brazil. *Scientific Reports*, *11*(1), 7704. https://doi.org/10.1038/s41598-021-87033-0

Wang, M., Li, T., & Jiang, L. (2016). Monitoring reclaimed lands subsidence in Hong Kong with InSAR technique by persistent and distributed scatterers. *Natural Hazards*, *82*(1), 531–543. https://doi.org/10.1007/s11069-016-2196-1

Wdowinski, S., Oliver-Cabrera, T., & Fiaschi, S. (2020). Land subsidence contribution to coastal flooding hazard in southeast Florida. *Proceedings of the International Association of Hydrological Sciences*, *382*, 207–211. https://doi.org/10.5194/piahs-382-207-2020

Weston, R. F. (1998). Final tech support doc for class II-B groundwater reclass petition Elizabeth port authority marine terminal. Retrieved from https://sharepoint.ourpassaic.org/Newark%20Bay%20Phase%20I%20Remedial%20Investigation%20Work%20Pla/RIWP%20Volume%201a%20of%203/Appendix%20C%20Water%20Data/Final%20Tech%20Support%20Doc%20for%20Class%20II-B%20Groundwater%20Reclass%20Petition%20Elizabeth%20Port%20Authority%20Marine.pdf

Wood, R. H. (1958). The stability of tall buildings. *Proceedings–Institution of Civil Engineers*, *11*(1), 69–102. https://doi.org/10.1680/iicep.1958.2424

Zaenal Putra, M. H., Suhadha, A. G., Hermawan, W., Sarah, D., Handika, R., Soebowo, E., & Satriyo, N. A. (2024). Assessing regional surface subsidence and its impact on critical infrastructure in Gedebage, Bandung using SBAS InSAR analysis. In *2024 IEEE international conference on aerospace electronics and remote sensing technology (ICARES)* (pp. 1–6). https://doi.org/10.1109/ICARES64249.2024.10767940

Zheng, Y., Peng, J., Li, C., Chen, X., Peng, Y., Ma, X., & Huang, M. (2024). Long-term SAR data analysis for subsidence monitoring and correlation study at Beijing Capital airport. *Remote Sensing*, *16*(3), 445. https://doi.org/10.3390/rs16030445

Zhuo, G., Dai, K., Huang, H., Li, S., Shi, X., Feng, Y., et al. (2020). Evaluating potential ground subsidence geo-hazard of Xiamen Xiang'an new airport on reclaimed land by SAR interferometry. *Sustainability*, *12*(17), 6991. https://doi.org/10.3390/su12176991